

# Small-Signal Modeling and Design of Phase-Locked Loops Using Harmonic Signal-Flow Graphs

Shahil Shah, *Member, IEEE*, Przemyslaw Koralewicz, *Member, IEEE*, Vahan Gevorgian, *Senior Member, IEEE*, and Leila Parsa, *Senior Member, IEEE*

**Abstract**—This paper introduces signal-flow graphs for linear time-periodic systems to streamline and visually describe the frequency-domain modeling of complex phase-locked loop (PLL) systems used in grid-connected converters. Small-signal modeling using the proposed graphs is demonstrated for two commonly used single-phase PLL structures: SOGI-PLL and Park-PLL. Loop-gain models are developed for these PLLs to evaluate how an orthogonal signal generator (OSG), which is required in single-phase PLLs using the synchronous reference frame (SRF) architecture, modifies the PLL loop gain compared to that of a three-phase SRF-PLL, which does not require an OSG. It is shown that the OSG in the SOGI-PLL and Park-PLL introduces a significant phase lag in the PLL loop gain, limiting the maximum bandwidth for which either PLL can be designed. Slow-frequency adaptation (SFA) of OSG is proposed to mitigate the influence of the OSG dynamics on the PLL loop gain. Experimental results are presented to validate the developed loop-gain models and show that the proposed SFA-SOGI-PLL and SFA-Park-PLL have better transient performance, they do not suffer from the bandwidth limit, and they preserve the steady-state performance of the standard SOGI-PLL and Park-PLL.

**Index Terms**—Linear time-periodic (LTP) systems, small-signal stability, phase-locked loops, impedance modeling.

## I. INTRODUCTION

NEW STABILITY problems such as control interactions and resonance have emerged in modern power systems with the high penetration of power electronics [1]–[4]. This has increased the importance of dynamic modeling of grid-connected power electronics equipment such as wind turbines, PV and storage inverters, HVDC and FACTS devices, etc. Modeling of grid-connected converters is difficult because they involve time-periodic quantities, and hence their linearized dynamics often form a linear time-periodic (LTP) system instead of a linear time-invariant (LTI) system. The frequency-domain relationship between any two variables in an LTP system—for example, between the terminal voltages and currents of a device for impedance modeling—is an infinite-dimensional transfer matrix known as harmonic transfer function (HTF) [5], [6]. Two mathematically equivalent modeling methods are used to derive HTF models of converters: harmonic linearization method [7]–[10] and harmonic state-space (HSS) method [11]–[13]. Modeling complexity increases exponentially using both methods for

converter topologies with rich circuit and control dynamics, such as modular multilevel converters [14].

Modeling using the HSS method results in models that are functions of high-dimensional state-space matrices [11], [12]; individual control functions do not appear as independent units in the final model, making the model difficult to use for control design [11], [12]. The harmonic linearization method, on the other hand, directly shows how each control function affects the final model, making it suitable for design-oriented analysis [15]. It can also be used with some modifications for large-signal modeling to predict the magnitude of resonance-generated oscillations or interharmonics. [16]–[18]; modeling using the harmonic linearization method, however, is not straight-forward because it requires analytically tracing a sinusoidal perturbation through highly nonlinear circuit and control system of a converter such as a complex phase-locked loop (PLL) structure. Dynamics such as coupling with the ac and dc networks at the converter terminals, frequency cross-coupling effects, and slow control functions are often ignored based on intuition without realizing their importance or an ability to add them if needed at a later stage [1]. This paper introduces signal-flow graphs for LTP systems to streamline the modeling using harmonic linearization method by visually describing the flow of perturbations through grid-connected converters. Such graphs are called “harmonic signal-flow graphs” because the frequencies of nodes in the graph are separated by multiples of the fundamental frequency. The structure of harmonic signal-flow graphs inspires understanding of how different control functions interact with each other and influence the dynamic behavior of a converter. For example, such graphs visually demonstrate different paths an injected perturbation flows through, giving insights on how each control function shapes the impedance response of the converter, which are very useful for control design to mitigate different types of stability problems. In this paper, the modeling using harmonic signal-flow graphs is demonstrated for two commonly used single-phase PLL structures based on the synchronous reference frame (SRF) architecture.

Modeling of a single-phase SRF-PLL is more complicated than a three-phase SRF-PLL because it requires a signal orthogonal to the input single-phase voltage to transform the input voltage to a rotating reference frame [19]. Different orthogonal signal generators (OSG) are presented in the literature [20]. Among them, delay-based OSG have the simplest implementation, but they suffer from poor steady-state performance and stability properties [21]. Second order generalized integrator (SOGI) and back-to-back Park transformation are more commonly used OSG methods owing to their superior performance and simpler implementation [20], [22]. Specifically, SOGI is the core building block of many advanced PLLs used for tracking harmonics in addition to the

S. Shah, P. Koralewicz, and V. Gevorgian are with the National Renewable Energy Laboratory (NREL), Golden, CO 80401, USA. Email: Shahil.Shah@nrel.gov

L. Parsa is with the University of California, Santa Cruz, CA 95064 USA.

fundamental component of the grid voltage [23], [24]. These advanced PLLs have been modeled in the time domain by approximating periodic ac variables by their steady-state values [21]–[26]; this has limited the understanding of instabilities experienced when a PLL is designed for a bandwidth higher than a few tens of hertz [22], [26]. Additionally, the time-domain modeling and ensuing assumptions do not reveal differences between the dynamics of PLLs using the SOGI and back-to-back Park’s transformation-based OSG. This has resulted in a misconception that the so-called SOGI-PLL and Park-PLL—which use SOGI and back-to-back Park’s transformation-based OSG, respectively—have identical dynamics [22]. This paper shows that even though the gains of both SOGI and back-to-back Park’s transformation-based OSG from the input voltage to the output orthogonal signals are identical, the PLLs using these OSG have different dynamic characteristics because of different frequency-locking mechanisms used by their respective OSGs.

This paper develops loop-gain models of single-phase SOGI-PLL and Park-PLL using harmonic signal-flow graphs and evaluates the influence of the OSG on the PLL loop gain. It is shown that in contrast to three-phase SRF-PLL, which does not require an OSG, single-phase SOGI-PLL and Park-PLL suffer from a significant phase lag in their loop gains because of their interaction with the OSG, limiting the maximum bandwidth for which they can be designed. To mitigate the bandwidth limit, a slow-frequency adaptation (SFA) mechanism is proposed for OSG. Experimental results are presented by implementing both the PLL structures on a dSPACE DS1104 controller board to validate their loop gain models and show that the proposed SFA approach improves transient performance and eliminates the bandwidth limit of both the PLLs without degrading their steady-state performance.

The paper is organized as follows: Section II introduces signal-flow graphs for LTP systems. Section III develops loop-gain models for single-phase SOGI-PLL and Park-PLL using harmonic signal-flow graphs. Section IV performs stability analysis of SOGI-PLL and Park-PLL using the developed loop-gain models. It shows that the bandwidth of these PLLs is limited because of interaction with the OSG. Section IV also presents SFA of OSG to eliminate the bandwidth limit and improve transient performance of both the PLLs. Section V concludes this paper.

## II. HARMONIC SIGNAL-FLOW GRAPHS

Harmonic signal-flow graphs are introduced by using them for the modeling of the Lossy Mathieu equation, a widely studied LTP system [6]:

$$\ddot{x}(t) + 2\xi\dot{x}(t) + k \cdot [1 - 2\beta\cos(2\pi f_1 t)] \cdot x(t) = 0 \quad (1)$$

Fig. 1a) represents the Lossy Mathieu equation as a feedback loop; its loop-gain can be used to study the stability of the equation. To obtain the loop gain, when a sinusoidal perturbation is injected in  $v$  (ref. Fig. 1) at an arbitrary frequency  $f_p$ ,  $w$  will have response at frequencies  $f_p$  and  $f_p \pm f_1$ . This is because the time-varying gain  $[1 - 2\beta\cos(2\pi f_1 t)]$  contains a constant as well as a periodic component with frequency  $f_1$ . After feedback through gain  $-k$ , the perturbation in  $w$  generates components at frequencies  $f_p \pm f_1$  in  $v$  in addition to the injected frequency  $f_p$ . This feedback reaction results in an infinite number of perturbation components at frequencies

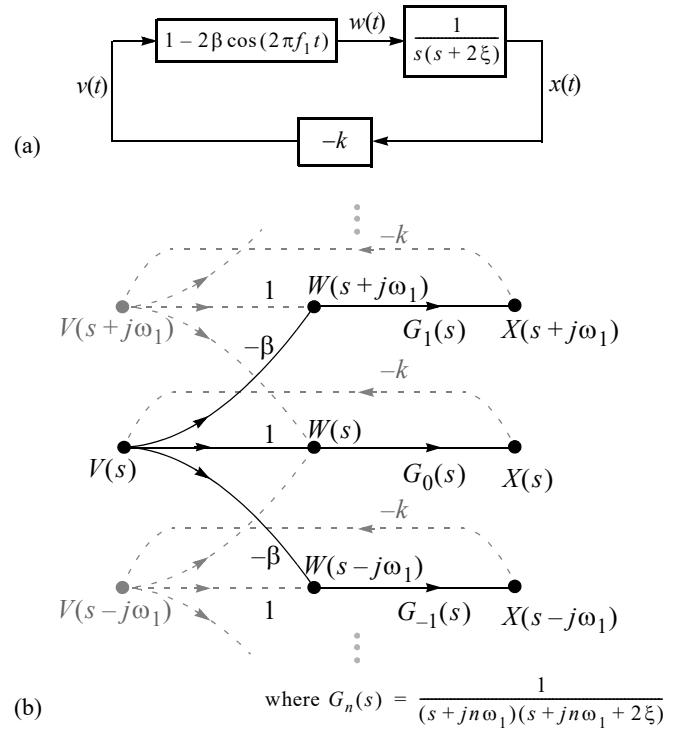


**Fig. 1.** Lossy Mathieu equation: (a) feedback loop representation and (b) harmonic signal-flow graph. Note  $\omega_1 = 2\pi f_1$  and  $s = j2\pi f_1$ .

$f_p \pm n \cdot f_1$ , where  $n$  is any nonnegative integer. The flow of the perturbation components is described using a signal-flow graph, as shown in Fig. 1b).

- 1) Nodes representing perturbation in a particular variable at different frequencies are kept on the same vertical line.
- 2) Nodes representing perturbation at a particular frequency in different variables are kept on the same horizontal line.

Gains of the horizontal branches between the nodes of  $v$  and  $w$  are unity, whereas the gains of the transverse branches between the nodes of  $v$  and  $w$  whose frequencies are separated by  $f_1$  are equal to  $-\beta$ . These statements are followed from the block diagram in Fig. 1a). Gains of branches between the nodes of other variables can be similarly obtained. Even though there is only one physical loop in Fig. 1b), the LTP nature results in multiple loops in Fig. 1a). Hence, the loop gain is a HTF describing the frequency-domain relationship between  $v$  and  $x$ . It is obtained in (2) at the top of the next page using the graph in Fig. 1b). The same relationship is developed in [6] using much less intuitive HSS method.

Note that the gains of mirror branches in a harmonic signal-flow graph are related as shown below:

$$\text{if } \frac{Y(s + ja)}{X(s + jb)} = G(s), \text{ then } \frac{Y(s - ja)}{X(s - jb)} = G(-s)^* \quad (3)$$

## III. MODELING OF SOGI-PLL AND PARK-PLL

Fig. 2 shows the implementation of SOGI-PLL and Park-PLL. Park’s transformation in (4) is used to transform variables from a stationary  $\alpha\beta$ -frame to rotating dq-frame:

$$\begin{bmatrix} \vdots \\ X(s + j2\omega_1) \\ X(s + j\omega_1) \\ X(s) \\ X(s - j\omega_1) \\ X(s - j2\omega_1) \\ \vdots \end{bmatrix} = \begin{bmatrix} \ddots & \vdots & \vdots & \vdots & \vdots & \vdots & \ddots \\ \cdots & G_2(s) & -\beta G_2(s) & 0 & 0 & 0 & \cdots \\ \cdots & -\beta G_1(s) & G_1(s) & -\beta G_1(s) & 0 & 0 & \cdots \\ \cdots & 0 & -\beta G_0(s) & G_0(s) & -\beta G_0(s) & 0 & \cdots \\ \cdots & 0 & 0 & -\beta G_{-1}(s) & G_{-1}(s) & -\beta G_{-1}(s) & \cdots \\ \cdots & 0 & 0 & 0 & -\beta G_{-2}(s) & -\beta G_{-2}(s) & \cdots \\ \ddots & \vdots & \vdots & \vdots & \vdots & \vdots & \ddots \end{bmatrix} \begin{bmatrix} \vdots \\ V(s + j2\omega_1) \\ V(s + j\omega_1) \\ V(s) \\ V(s - j\omega_1) \\ V(s - j2\omega_1) \\ \vdots \end{bmatrix} \quad (2)$$

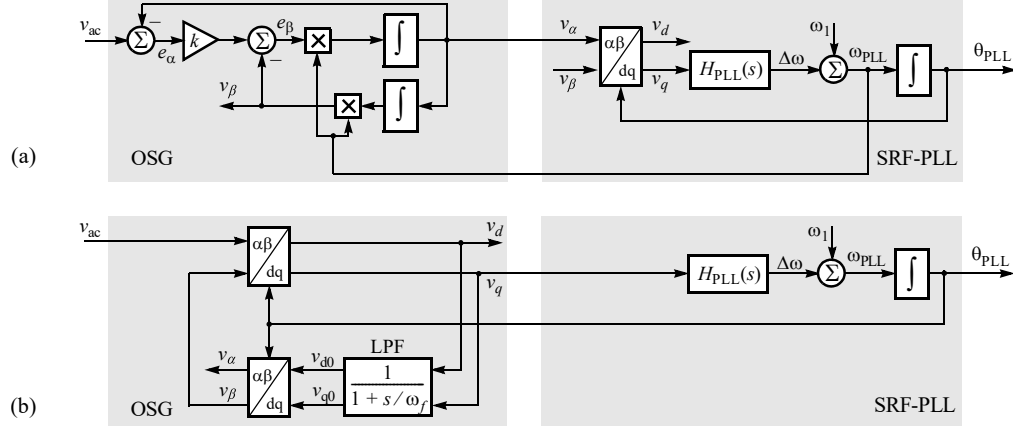


Fig. 2. Synchronous reference frame-based single-phase PLLs: (a) SOGI-PLL and (b) Park-PLL.

$$\begin{bmatrix} v_d \\ v_q \end{bmatrix} = \begin{bmatrix} \cos \theta_{PLL} & \sin \theta_{PLL} \\ -\sin \theta_{PLL} & \cos \theta_{PLL} \end{bmatrix} \begin{bmatrix} v_\alpha \\ v_\beta \end{bmatrix} \quad (4)$$

where  $\theta_{PLL}$  is the PLL output angle.

For SOGI-PLL, the relationship between the SOGI-based OSG input  $v_{ac}$  and outputs  $v_\alpha$  and  $v_\beta$  is [19]:

$$\frac{V_\alpha(s)}{V_{ac}(s)} = \frac{k\omega_1 s}{s^2 + k\omega_1 s + \omega_1^2} \equiv G_\alpha(s) \quad (5)$$

$$\frac{V_\beta(s)}{V_{ac}(s)} = \frac{k\omega_1^2}{s^2 + k\omega_1 s + \omega_1^2} \equiv G_\beta(s) \quad (6)$$

where  $k$  is the SOGI gain, which is kept  $\sqrt{2}$  in this paper to achieve critical damping of the transfer function gains in (5) and (6). Fig. 3 shows the response of these gains; note that  $G_\alpha(s)$  and  $G_\beta(s)$  have unity gain and, respectively, the phase of  $0^\circ$  and  $-90^\circ$  at the fundamental frequency  $f_1$ . Hence, the input voltage,  $v_{ac}$ , at the fundamental frequency  $f_1$  gives the desired orthogonal signals  $v_\alpha$  and  $v_\beta$  for using them in the SRF-PLL block (ref. Fig. 2a). The back-to-back Park's transformation-based OSG in the Park-PLL has the same gains as in (5) and (6) when the corner frequency  $\omega_f$  of the low-pass filter shown in Fig. 2b) is kept equal to  $k \cdot \omega_1$  [22]. Hence,  $\omega_f$  is kept 533 rad/s. This equivalence between the SOGI and Park's transformation-based OSGs has resulted in a misconception that the SOGI-PLL and Park-PLL have identical small-signal dynamics [19].

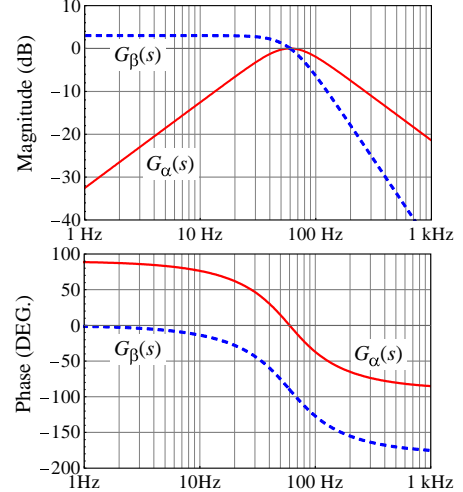
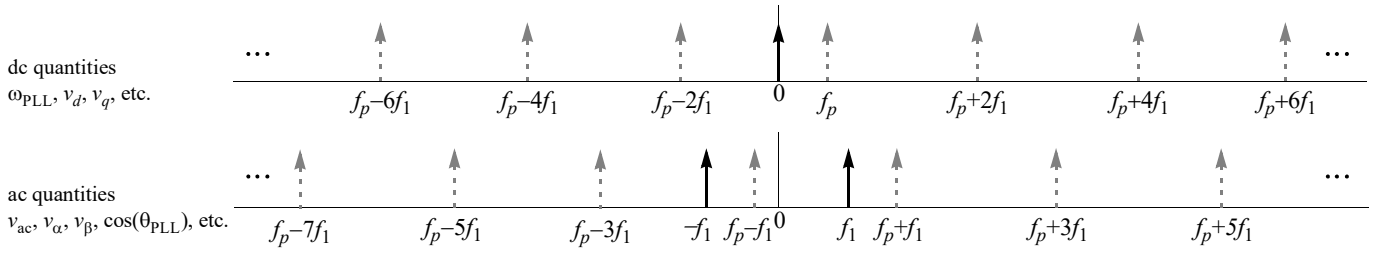


Fig. 3. Gains of SOGI-based OSG from the input voltage,  $v_{ac}$ , to output signals,  $v_\alpha$  and  $v_\beta$ .

Table I shows compensator  $H_{PLL}(s)$  for different bandwidth designs used for the experimental and analytical case studies presented in this paper. To maintain uniformity for comparison, the PLL compensators in Table I are designed to provide the same phase margin of  $45^\circ$  while ignoring the OSG dynamics [19]; i.e., for designing these compensators, the loop gain of both the SOGI-PLL and Park-PLL is assumed to be the same as that of the standard three-phase SRF-PLL:  $V_1 \cdot H_{PLL}(s)/s$ . It will be shown later that the ignored OSG dynamics introduce a significant phase lag in the PLL loop gain and destabilize the PLL if it is designed for a



**Fig. 4.** Spectrum of PLL variables under small-signal perturbation. Solid arrows indicate steady-state components, and dashed arrows indicate small-signal linear components that appear when a small-signal sinusoidal perturbation is injected in  $\omega_{PLL}$  at frequency  $f_p$ . Note that the mirror images of the perturbation components are not shown for clarity.

TABLE I: PLL COMPENSATOR FOR DIFFERENT BANDWIDTH DESIGNS

Bandwidth (Hz)	$H_{PLL}(s)$
20	$0.52 + 65.68/s$
30	$0.78 + 147.78/s$
40	$1.04 + 262.73/s$
50	$1.30 + 410.52/s$
60	$1.56 + 591.151/s$
200	$5.22 + 6568.34/s$

TABLE II: FREQUENCIES OF PERTURBATION COMPONENTS

PLL Variables	Frequency
ac quantities: $v_{ac}, v_{\alpha}, v_{\beta}, e_{\alpha}, e_{\beta},$ and $\cos(\theta_{PLL})$	$f_p \pm n \cdot f_1$ ( $n \in$ odd integers)
dc quantities: $\omega_{PLL}, v_d, v_q, v_{d0}$ and $v_{q0}$	$f_p \pm n \cdot f_1$ ( $n \in$ even integers)

bandwidth above a certain limit. The grid voltage amplitude,  $V_1$ , and frequency,  $f_1$ , are 170 V and 60 Hz, respectively.

The loop-gain  $L(s)$  of SRF-based PLLs is the product of the transfer function from the PLL frequency,  $\omega_{PLL}$ , to q-axis voltage,  $v_q$ , and the PLL compensator,  $H_{PLL}(s)$ :

$$L(s) = -\frac{V_q(s)}{\Omega_{PLL}(s)} \cdot H_{PLL}(s) \quad (7)$$

where  $V_q(s)$  and  $\Omega_{PLL}(s)$  denote the Laplace transforms, respectively, of the time-domain signals  $v_q$  and  $\omega_{PLL}$ . The negative sign in (7) is included so that negative-feedback loop can be assumed while using the loop-gain response for designing  $H_{PLL}(s)$ .

#### A. Spectrum of PLL Variables Under Perturbation

Based on (7), the loop gain of the SOGI-PLL and Park-PLL can be obtained by obtaining the linear response in  $v_q$  when a sinusoidal perturbation is injected in  $\omega_{PLL}$ . When a sinusoidal perturbation is injected in  $\omega_{PLL}$  at frequency  $f_p$ , because of the time-periodic nature of the dynamics of these PLLs, multiple perturbation components will appear in the PLL variables at frequencies  $m \cdot f_p \pm n \cdot f_1$  [1], where  $f_1$  is the fundamental frequency. Nonlinear components with ‘m’ other than unity can be ignored for the small-signal modeling. Moreover, it can be shown that the linear components at

frequencies  $f_p \pm n \cdot f_1$  appear in the ac and dc variables only for alternate values of n, as shown in Table II. This is inferred by tracing the injected perturbation in  $\omega_{PLL}$  through the PLL circuit. For instance, the perturbation in  $\omega_{PLL}$  of the SOGI-PLL in Fig. 2a) at frequency  $f_p$  will produce perturbations in  $v_{\alpha}$  and  $v_{\beta}$  at frequencies  $f_p \pm f_1$  because of the multiplication in the SOGI block with ac signals at the fundamental frequency  $f_1$ . After going through Park’s transformation, these components will, in turn, produce perturbation in  $v_d, v_q$ , and  $\omega_{PLL}$  at frequencies  $f_p$  and  $f_p \pm 2 \cdot f_1$ . Following through this feedback reaction, it can be shown that the perturbation appears in the ac and dc variables at frequencies  $f_p \pm n \cdot f_1$  with n being even integers for dc variables and odd integers for ac variables. Similarly, for developing the transfer function gains from the input voltage,  $v_{ac}$ , to PLL outputs ( $v_d, v_q, \omega_{PLL}, \cos(\theta_{PLL}),$  etc.), it can be shown that the response in the input voltage,  $v_{ac}$ , at frequencies  $f_p \pm n \cdot f_1$  is decoupled for n being even and odd integers. In other words, considering the perturbation in  $v_{ac}$  at frequencies  $f_p \pm n \cdot f_1$  with  $n \in$  even integers is redundant, i.e., the resulting harmonic signal-flow graph is disconnected from the graph showing the flow of perturbation in  $v_{ac}$  at frequencies  $f_p \pm n \cdot f_1$  with  $n \in$  odd integers [3]. Based on this discussion, the spectrum of the PLL variables during small-signal perturbation is shown in Fig. 4.

#### B. SOGI-PLL

Based on the spectrum of the PLL variables in Fig. 4 during the small-signal perturbation and the SOGI-PLL structure in Fig. 2a), the harmonic signal-flow graph of the SOGI-PLL can be drawn as shown in Fig. 5. To obtain the PLL loop gain as defined in (7), the branches between the nodes of  $v_q$  and  $\omega_{PLL}$  are ‘‘opened’’ by removing the compensator  $H_{PLL}(s)$  (these branches are represented with small rectangles). Additionally, we model only a part of the graph drawn using solid lines. This is equivalent to considering only the  $f_p$  perturbation component in the dc variables and  $f_p \pm f_1$  perturbation components in the ac variables.

To obtain the gains of the branches from  $\Omega_{PLL}(s)$  to  $V_{\alpha\beta}(s \pm j\omega_1)$ , corresponding time-domain variables, including steady-state and small-signal perturbations, can be written as:

$$\omega_{PLL}(t) = \omega_1 + \hat{\Omega}_s \cos(2\pi f_p t + \varphi_{\omega s}) \quad (8)$$

$$v_{\alpha}(t) = V_1 \cos(2\pi f_1 t) + \hat{V}_{\alpha p} \cos[2\pi(f_p + f_1)t + \varphi_{v\alpha p}] + \hat{V}_{\alpha n} \cos[2\pi(f_p - f_1)t + \varphi_{v\alpha n}] \quad (9)$$

$$v_{\beta}(t) = V_1 \sin(2\pi f_1 t) + \hat{V}_{\beta p} \cos[2\pi(f_p + f_1)t + \varphi_{v\beta p}] + \hat{V}_{\beta n} \cos[2\pi(f_p - f_1)t + \varphi_{v\beta n}] \quad (10)$$

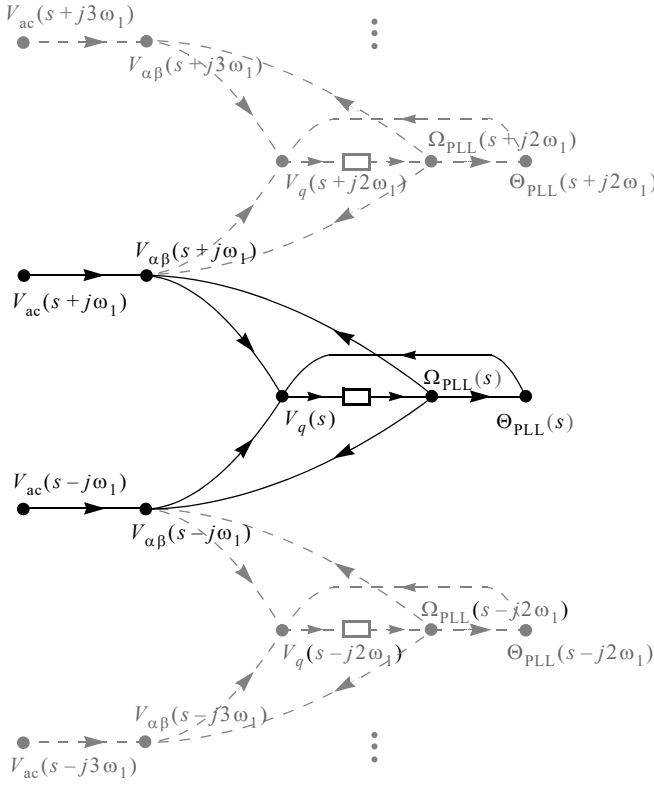


Fig. 5. Harmonic signal-flow graph of SOGI-PLL.

“Hat” in (8)–(10) signifies the small-signal nature of the perturbation components. Note that the fundamental component of  $v_\alpha$  is in phase with the input voltage,  $v_{ac}$ , and that of  $v_\beta$  lags by  $90^\circ$ .

$\omega_{PLL}$ ,  $v_\alpha$  and  $v_\beta$  can be written in the frequency-domain as:

$$\mathbf{\Omega}_{PLL}[f] = \begin{cases} \omega_1, & f = 0 \\ \mathbf{\Omega}_s, & f = \pm f_p \end{cases} \quad (11)$$

$$\mathbf{V}_\alpha[f] = \begin{cases} V_1/2, & f = \pm f_1 \\ \mathbf{V}_{ap}, & f = \pm(f_p + f_1) \\ \mathbf{V}_{an}, & f = \pm(f_p - f_1) \end{cases} \quad (12)$$

$$\mathbf{V}_\beta[f] = \begin{cases} \mp jV_1/2, & f = \pm f_1 \\ \mathbf{V}_{bp}, & f = \pm(f_p + f_1) \\ \mathbf{V}_{bn}, & f = \pm(f_p - f_1) \end{cases} \quad (13)$$

where  $\mathbf{\Omega}_s = (\hat{\Omega}_s/2)e^{\pm j\varphi_{os}}$ . The Fourier coefficients  $\mathbf{V}_{ap}$ ,  $\mathbf{V}_{an}$ ,  $\mathbf{V}_{bp}$ , and  $\mathbf{V}_{bn}$  follow similar shorthand notations. Based on (11)–(13) and Fig. 2(a), the Fourier components of the error signal  $e_\beta$  can be obtained as:

$$\mathbf{E}_\beta[f] = \begin{cases} \pm jV_1/2, & f = \pm f_1 \\ -(k \cdot \mathbf{V}_{ap} + \mathbf{V}_{bp}), & f = \pm(f_p + f_1) \\ -(k \cdot \mathbf{V}_{an} + \mathbf{V}_{bn}), & f = \pm(f_p - f_1) \end{cases} \quad (14)$$

Based on the SOGI block implementation in Fig. 2(a), the components of  $v_\alpha$  and  $v_\beta$  at frequencies  $\pm(f_p \pm f_1)$  can be obtained in terms of the components of  $\omega_{PLL}$  and  $e_\beta$  from (11) and (14) as:

$$\mathbf{V}_\alpha[\pm(f_p + f_1)] = \frac{1}{\pm 2\pi(f_p + f_1)} \left[ \pm \frac{V_1}{2} \mathbf{\Omega}_s + j\omega_1(k \cdot \mathbf{V}_{ap} + \mathbf{V}_{bp}) \right] \quad (15)$$

$$\mathbf{V}_\beta[\pm(f_p + f_1)] = \pm \frac{V_1}{2} \left\{ \frac{1}{j\omega_1} - \frac{j\omega_1}{[2\pi(f_p + f_1)]^2} \right\} \mathbf{\Omega}_s + \left[ \frac{\omega_1}{2\pi(f_p + f_1)} \right]^2 (k \cdot \mathbf{V}_{ap} + \mathbf{V}_{bp}) \quad (16)$$

Comparing (15) and (16) with (12) and (13),  $\mathbf{V}_{ap}$  and  $\mathbf{V}_{bp}$  can be written in terms of  $\mathbf{\Omega}_s$ , giving the following gains:

$$\frac{V_\alpha(s + j\omega_1)}{\mathbf{\Omega}_{PLL}(s)} = j \frac{V_1}{k \cdot \omega_1} G_\alpha(s + j\omega_1) \quad (17)$$

$$\frac{V_\beta(s + j\omega_1)}{\mathbf{\Omega}_{PLL}(s)} = j \frac{V_1}{k \cdot \omega_1} G_\beta(s + j\omega_1) - j \frac{V_1}{2 \cdot \omega_1} \quad (18)$$

Using the relationship between mirror branches from (3), the following gains are obtained from (17) and (18):

$$\frac{V_\alpha(s - j\omega_1)}{\mathbf{\Omega}_{PLL}(s)} = -j \frac{V_1}{k \cdot \omega_1} G_\alpha(s - j\omega_1) \quad (19)$$

$$\frac{V_\beta(s - j\omega_1)}{\mathbf{\Omega}_{PLL}(s)} = -j \frac{V_1}{k \cdot \omega_1} G_\beta(s - j\omega_1) + j \frac{V_1}{2 \cdot \omega_1} \quad (20)$$

Eq. (17)–(20) give linear response in  $v_\alpha$  and  $v_\beta$  at frequencies  $f_p \pm f_1$  because of the perturbation in  $\omega_{PLL}$  at frequency  $f_p$ .

Based on Fig. 5, the next step to obtain the SOGI-PLL loop gain requires developing the response in  $v_q$  at frequency  $f_p$  because of the perturbation in  $v_\alpha$  and  $v_\beta$  at frequencies  $f_p \pm f_1$  and in  $\theta_{PLL}$  at frequency  $f_p$ . Although the perturbations in  $v_\alpha$ ,  $v_\beta$ , and  $\theta_{PLL}$  affect  $v_q$  through the same Park’s transformation shown in Fig. 2(a), their effects can be modeled independently using the superposition principle. Applying Park’s transformation (4) to  $v_\alpha$  and  $v_\beta$  in (9) and (10) while ignoring the perturbation in  $\theta_{PLL}$  (i.e., assuming  $\theta_{PLL} = \theta_1$ ), the response in  $v_q$  at frequency  $f_p$  can be obtained as:

$$v_q(t) = \frac{\hat{V}_{ap}}{2} \sin(2\pi f_p t + \varphi_{vap}) + \frac{\hat{V}_{bp}}{2} \cos(2\pi f_p t + \varphi_{vbp}) - \frac{\hat{V}_{an}}{2} \sin(2\pi f_p t + \varphi_{van}) + \frac{\hat{V}_{bn}}{2} \cos(2\pi f_p t + \varphi_{vbn}) \quad (21)$$

The gains of branches from  $V_\alpha(s \pm j\omega_1)$  and  $V_\beta(s \pm j\omega_1)$  to  $V_q(s)$  in the harmonic signal-flow graph are obtained by comparing the Fourier components of  $v_q$  in (21) with (12) and (13). Additionally, linearizing the Park’s transformation, the gain of the branch from  $\theta_{PLL}(s)$  to  $V_q(s)$  in Fig. 5 can be obtained as  $-V_1$ . Hence, the total response in  $v_q$  at frequency  $f_p$  is found to be:

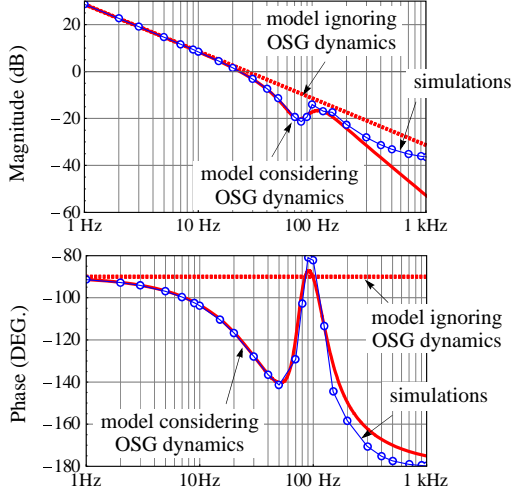


**Fig. 6.** Response of the loop gain of SOGI-PLL excluding the compensator  $H_{PLL}(s)$ . Solid lines: model considering the dynamics of SOGI-based OSG; dashed-lines: model ignoring the SOGI dynamics; circles: point-by-point simulations.

$$V_q(s) = \begin{bmatrix} -\frac{j}{2} & \frac{j}{2} & \frac{1}{2} & \frac{1}{2} \end{bmatrix} \begin{bmatrix} V_\alpha(s+j\omega_1) \\ V_\alpha(s-j\omega_1) \\ V_\beta(s+j\omega_1) \\ V_\beta(s-j\omega_1) \end{bmatrix} - V_1 \cdot \frac{\Omega_{PLL}(s)}{s} \quad (22)$$

Using (17)–(20) in (22), the desired transfer function from  $\omega_{PLL}$  to  $v_q$  is obtained as:

$$\frac{V_q(s)}{\Omega_{PLL}(s)} = -\frac{V_1}{s} \left[ \frac{G_\alpha(s+j\omega_1) + G_\alpha(s-j\omega_1)}{2} \right] \quad (23)$$

Based on (7), the SOGI-PLL loop gain excluding the compensator  $H_{PLL}(s)$  is negative of the gain developed in (23). Fig. 6 validates the loop-gain response obtained using the developed model against point-by-point simulations. It also shows the response of the model ignoring the SOGI block dynamics, which is equivalent to assuming  $G_\alpha(s)$  to be unity in (23). It is evident that the SOGI-based OSG introduces significant phase lag, limiting the maximum bandwidth of an SOGI-PLL to a few tens of Hertz. The model in (23) shows that the loop gain depends on the SOGI-based OSG design in a more sophisticated manner than as interpreted in [22] by a first-order low-pass filter.

### C. Park-PLL

The harmonic signal-flow graph of the Park-PLL is drawn in Fig. 7 based on the implementation in Fig. 2b) and the spectrum of PLL variables during perturbation from Fig. 4. First, we consider only the solid branches in the graph. Gains of individual branches can be derived using the harmonic linearization method by following the same procedure as the SOGI-PLL. The developed gains of the solid branches are listed in Table III. The transfer function from  $\Omega_{PLL}(s)$  to  $V_q(s)$  is obtained by solving the graph:

$$\frac{V_q(s)}{\Omega_{PLL}(s)} = -\frac{V_1}{s} \left[ \frac{1 + \frac{s}{\omega_f}}{1 + \frac{s}{(\omega_f/2)}} \right] \quad (24)$$

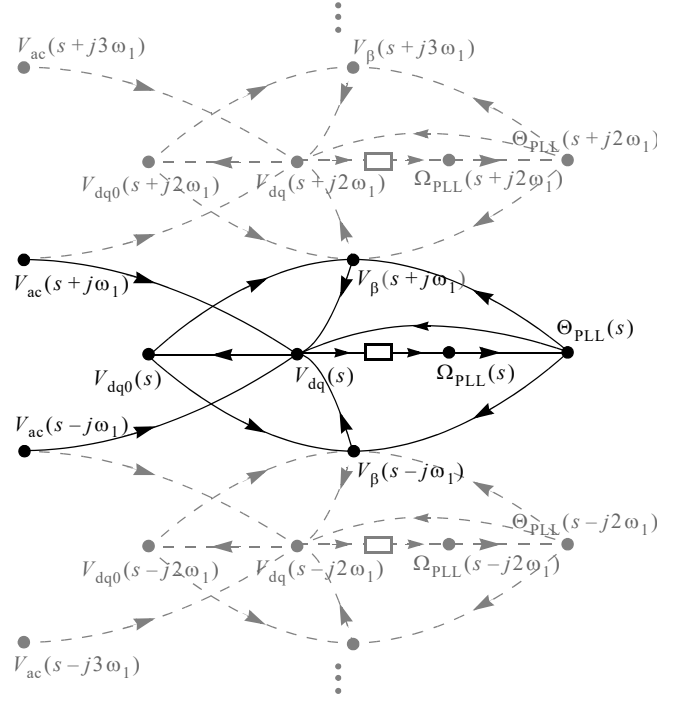


**Fig. 7.** Harmonic signal-flow graph of Park-PLL.

**TABLE III:** GAINS OF BRANCHES IN THE HARMONIC SIGNAL-FLOW GRAPH OF PARK-PLL

Source Node	Sink Node	Gain <sup>a</sup>
$\Omega_{PLL}(s)$	$\Theta_{PLL}(s)$	$1/s$
$\Theta_{PLL}(s)$	$V_{dq}(s)$	$[0 \quad -V_1]^T$
$\Theta_{PLL}(s)$	$V_\beta(s+j\omega_1)$	$V_1/2$
$\Theta_{PLL}(s)$	$V_\beta(s-j\omega_1)$	$V_1/2$
$V_{dq}(s)$	$V_{dq0}(s)$	$\begin{bmatrix} 1/(1+s/\omega_f) & 0 \\ 0 & 1/(1+s/\omega_f) \end{bmatrix}$
$V_{dq0}(s)$	$V_\beta(s+j\omega_1)$	$[-j/2 \quad 1/2]$
$V_{dq0}(s)$	$V_\beta(s-j\omega_1)$	$[j/2 \quad 1/2]$
$V_\beta(s+j\omega_1)$	$V_{dq}(s)$	$[j/2 \quad 1/2]^T$
$V_\beta(s-j\omega_1)$	$V_{dq}(s)$	$[-j/2 \quad 1/2]^T$

a. where  $V_{dq}(s) \equiv [V_d(s) \quad V_q(s)]^T$ .

The Park-PLL loop gain excluding the compensator  $H_{PLL}(s)$  is the negative of the transfer function in (24). Fig. 8 compares the Park-PLL loop-gain response obtained using the model in (24) [long-dashed lines] and point-by-point simulations [circles]. Fig. 8 also shows the response of the model ignoring the OSG dynamics [short-dashed lines]. Clearly, the developed model better captures the Park-PLL dynamics. Nonetheless, the model still exhibits significant errors in capturing the phase lag introduced by the OSG. The model accuracy can be improved by considering additional branches represented using dashed lines in Fig. 7. Solid lines in Fig. 8 show the response of the updated model. As shown, the model accuracy has significantly improved. The gains of the

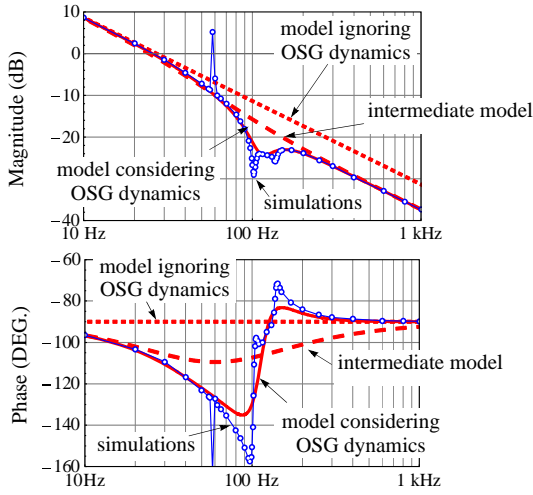


**Fig. 8.** Response of the loop gain of Park-PLL excluding the compensator  $H_{PLL}(s)$ . Solid lines: model using the harmonic signal-flow graph shown in Fig. 7; long-dashed-lines: model in (24), which considers only the solid branches of the harmonic signal-flow graph shown in Fig. 7; and short-dashed-lines: model ignoring the dynamics of the back-to-back Park's transformation-based OSG; circles: point-by-point simulations.

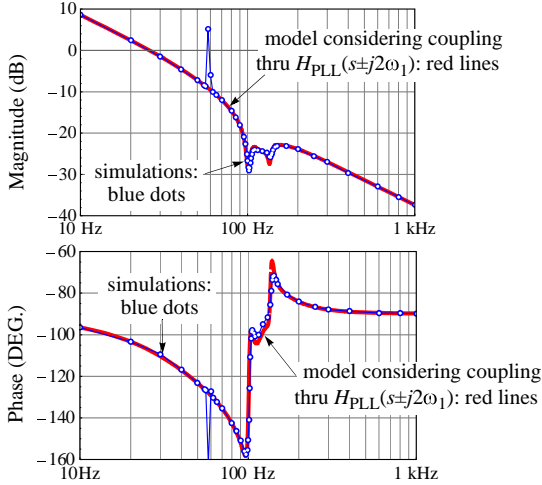


**Fig. 9.** Park-PLL loop gain excluding the compensator  $H_{PLL}(s)$ . Solid lines: model using the harmonic signal-flow graph in Fig. 7 while also considering the dependence on  $H_{PLL}(s \pm j2\omega_1)$  because of the frequency cross-coupling effects; circles: point-by-point simulation.

dashed branches are obtained directly from Table III based on the relationships between parallel and mirror branches of a harmonic signal-flow graph. It is increasingly difficult to manipulate equations when the additional dashed branches are considered in the modeling. Hence, the updated model is obtained by solving the signal-flow graph in Fig. 7 using a Mason's rule solver algorithm from [27] based on the symbolic toolbox of MATLAB.

Even after considering the dashed branches of the harmonic signal-flow graph, some errors persist in the model prediction in Fig. 8. The inaccuracy in the model prediction is because of the dependence of the transfer function from  $\Omega_{PLL}(s)$  to  $V_q(s)$  on  $H_{PLL}(s)$ , which is ignored by neglecting the flow of the perturbation components at  $f_p \pm 2f_1$  through the PLL compensator. The model prediction is exact, as shown in Fig. 9, when the coupling with  $H_{PLL}(s \pm j2\omega_1)$  is included in the input file to the signal-flow graph solver [27]. The signal-flow graph solver [27] showed that there

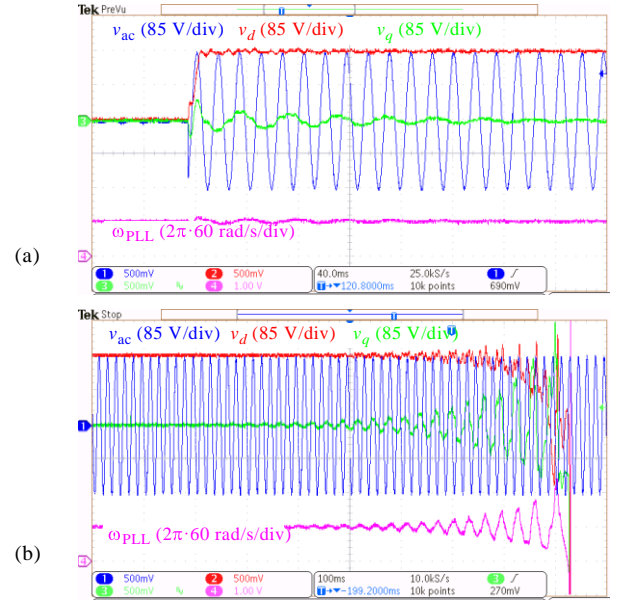


**Fig. 10.** Limitation on the bandwidth of SOGI-PLL. a) start-up transient of SOGI-PLL for 30 Hz bandwidth design; b) loss of stability when the bandwidth is increased to 40 Hz by updating the PLL compensator  $H_{PLL}(s)$  in real time.

are around 1000 loops of different orders in Fig. 7; obviously, it is not possible to manually manipulate such a complicated graph.

#### IV. SLOW-FREQUENCY ADAPTATION (SFA) OF ORTHOGONAL-SIGNAL GENERATORS

##### A. Bandwidth Limit of OSG-Based PLLs

Phase lag introduced by OSG in the loop gains of SOGI-PLL (ref. Fig. 6) and Park-PLL (ref. Fig. 8) limits the maximum bandwidth for which either PLL can be designed. For example, the bandwidth of the SOGI-PLL with the loop-gain response in Fig. 6 is limited to 35 Hz. Fig. 10a) shows the response of the SOGI-PLL implemented on a dSPACE controller board during start-up when  $H_{PLL}(s)$  is selected from Table I for 30 Hz bandwidth. The response in Fig. 10b) shows that the PLL loses stability when the compensator  $H_{PLL}(s)$  is updated in real time for a 40 Hz bandwidth design. For both cases, the PLL compensator is designed to give a  $45^\circ$  phase margin without considering the dynamics of the SOGI-based OSG; however, the interaction between the SOGI-based OSG and the SRF-PLL block pushes the phase margin to a low value and makes the SOGI-PLL unstable if designed for a bandwidth above 35 Hz. The bandwidth of the Park-PLL is similarly limited because of the interaction between back-to-back Park's transformation-based OSG and the SRF-PLL block. Fig. 11a) shows the start-up of the Park-PLL for a 50 Hz bandwidth design. Fig. 11b) shows that the PLL loses stability when the bandwidth is increased to 60 Hz by updating  $H_{PLL}(s)$  in real time.

##### B. SFA-SOGI-PLL

The OSG of a single-phase SRF-PLL requires estimation of the grid voltage frequency for accurately generating two orthogonal signals. As shown in Fig. 2(a), the frequency estimation input to OSG is provided in SOGI-PLL via feedback of  $\omega_{PLL}$  from the SRF-PLL block. This couples the dynamics of the SOGI-based OSG and the SRF-PLL block, which consequently modifies the loop gain of the single-phase SOGI-PLL from that of a three-phase

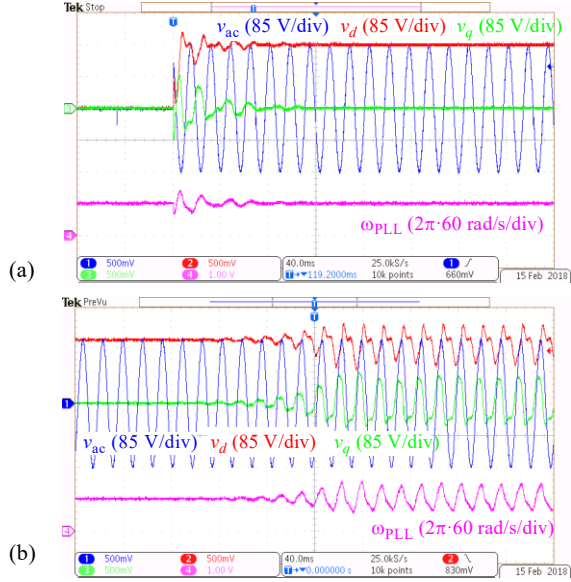


**Fig. 11.** Limitation on the bandwidth of a Park-PLL. a) start-up transient of a Park-PLL for 50 Hz bandwidth design; b) loss of stability when the bandwidth is increased to 60 Hz by updating the PLL compensator  $H_{PLL}(s)$  in real time.

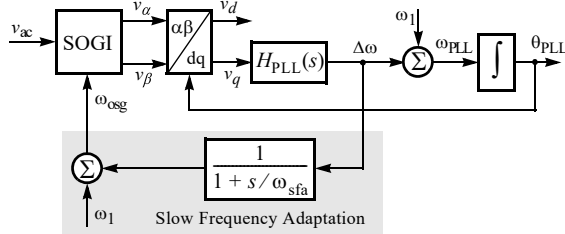


**Fig. 12.** Single-phase SOGI-PLL with slow frequency-adaptation (SFA) of SOGI-based OSG to mitigate phase lag in the PLL loop gain.

SRF-PLL. As shown by the developed model in the previous section, the coupling between the OSG and SRF-PLL blocks manifest as a significant phase lag in the PLL loop gain, limiting the bandwidth for which an SOGI-PLL can be designed.

From the harmonic signal-flow graph of the SOGI-PLL shown in Fig. 5, it can be inferred that if the branches from the nodes of  $\omega_{PLL}$  to  $v_{\alpha\beta}$  are removed, the interaction of the SOGI-based OSG with the SRF-PLL block is eliminated. This is achieved in [26] by eliminating the frequency estimation for the OSG by fixing its frequency input at the nominal frequency  $f_1$ ; however, this results in steady-state distortions whenever the actual frequency is different from the nominal frequency  $f_1$ . The dynamics of the SOGI-based OSG and the SRF-PLL block can be decoupled while preserving the frequency estimation to avoid steady-state distortions by using a low-pass filter in the frequency feedback from the SRF-PLL to the OSG. Implementation of the SOGI-PLL with the SFA of OSG using a low-pass filter is shown in Fig. 12. The transfer function from  $\omega_{PLL}$  to  $v_q$  of the updated PLL is:

$$\frac{V_q(s)}{\Omega_{PLL}(s)} = -\frac{V_1}{s} \left\{ 1 - \frac{1}{1 + \frac{s}{\omega_{sfa}}} \left[ 1 - \frac{G_\alpha(s + j\omega_1) + G_\alpha(s - j\omega_1)}{2} \right] \right\} \quad (25)$$

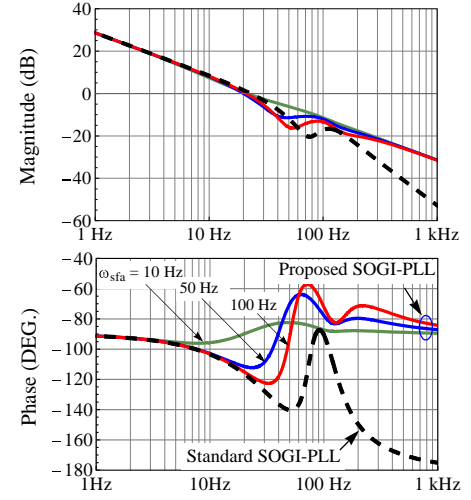


**Fig. 13.** Loop-gain response of standard SOGI-PLL and proposed SFA-SOGI-PLL with SFA of OSG. Loop-gain responses of the proposed SFA-SOGI-PLL are shown for different corner frequencies of the low-pass filter ( $\omega_{sfa}$ ) used for SFA.

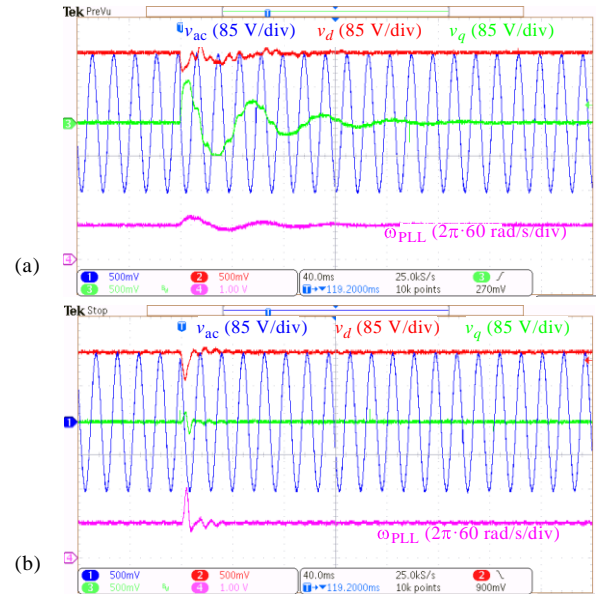


**Fig. 14.** Performance of SOGI-PLL during 45° phase jump: a) standard SOGI-PLL with 30 Hz bandwidth design [higher bandwidth is not possible for standard SOGI-PLL], b) SFA-SOGI-PLL with SFA loop and 200 Hz bandwidth design [SFA loop eliminates the bandwidth limit].

It is evident from (25) that the SFA reduces the effects of the OSG design on the PLL loop gain. Fig. 13 shows how SFA changes the loop gain of an SOGI-PLL for different corner frequencies,  $\omega_{sfa}$ , of the low-pass filter used for SFA. As expected, Fig. 13 shows that as the corner frequency  $\omega_{sfa}$  is reduced, the SOGI-PLL loop gain starts approaching that of a three-phase SRF-PLL, eliminating the bandwidth limit. Fig. 14 compares the performance during a phase jump of the standard SOGI-PLL (designed for 30 Hz bandwidth because it becomes unstable for higher bandwidths) and the SOGI-PLL with SFA loop (designed for 200 Hz bandwidth);  $\omega_{sfa}$  is  $2\pi \cdot 10$  rad/s for the responses in Fig. 14b).

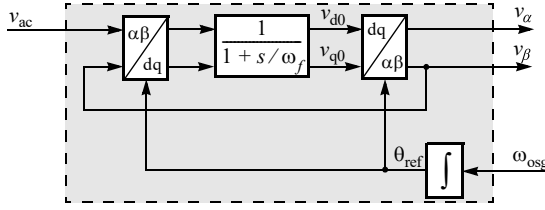


Fig. 15. OSG of the proposed SFA-Park-PLL.

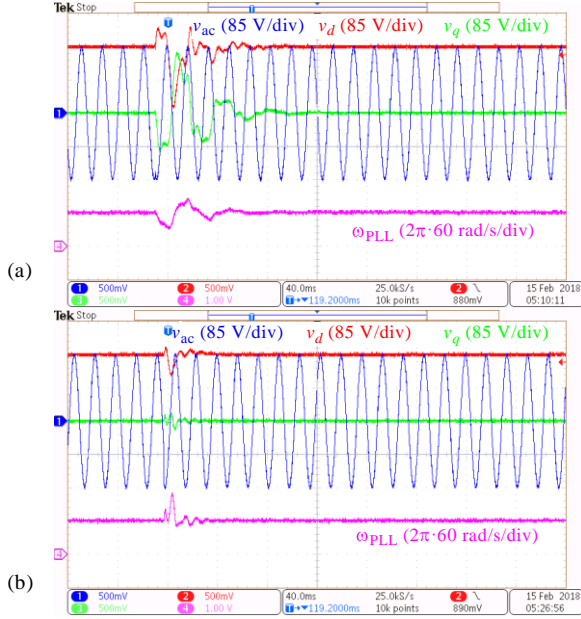


Fig. 16. Performance of Park-PLL during  $45^\circ$  phase jump: a) standard Park-PLL with 50 Hz bandwidth design [higher bandwidth is not possible for standard Park-PLL], b) Park-PLL with SFA of OSG and designed for 200 Hz bandwidth [SFA loop eliminates the bandwidth limit].

### C. SFA-Park-PLL

In contrast to SOGI-PLL, the back-to-back Park's transformation-based OSG in Park-PLL receives frequency estimation indirectly via feedback of  $\theta_{PLL}$ . Nonetheless, the same as SOGI-PLL, the frequency adaptation of OSG is the reason behind coupling between the OSG and SRF-PLL block. Because the frequency adaptation is achieved in an indirect manner in Park-PLL, the SFA cannot be implemented directly for the back-to-back Park's transformation-based OSG. Hence, the back-to-back Park's transformation-based OSG of the Park-PLL is modified as shown in Fig. 15 to make it compatible with the implementation of the SFA mechanism shown in Fig. 12. The modified OSG in Fig. 15 can be used in the place of SOGI block in Fig. 12 for realizing Park-PLL with SFA of its OSG. Fig. 16 compares the performance during a phase jump of the standard Park-PLL (designed for 50 Hz bandwidth since it becomes unstable for a higher bandwidth) with the proposed SFA-Park-PLL with SFA (designed for 200 Hz bandwidth).

Figs. 14 and 16 show that the proposed SFA-SOGI-PLL and SFA-Park-PLL with SFA of their OSG do not suffer from the bandwidth limit, and they have significantly improved transient performance compared to their standard counterparts.

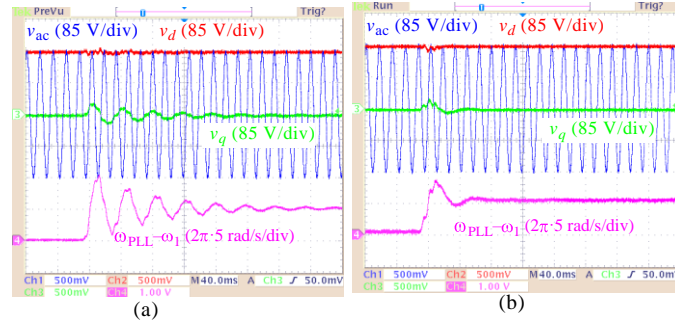


Fig. 17. Response during 5 Hz frequency jump: a) standard SOGI-PLL with 30 Hz bandwidth design and b) SFA-SOGI-PLL with 30 Hz bandwidth design.

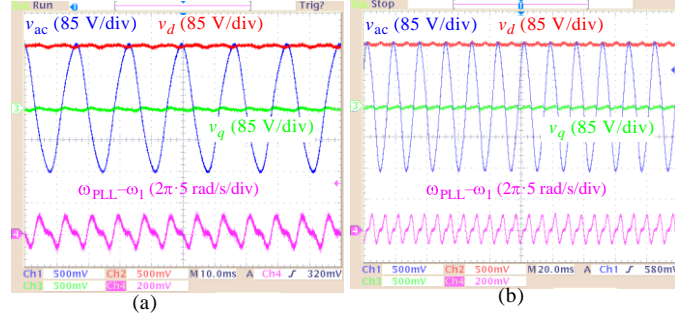


Fig. 18. Steady-state response in presence of 5% 3rd harmonic in the input voltage. a) standard SOGI-PLL and b) SFA-SOGI-PLL; both PLLs are designed for 30 Hz bandwidth.

### D. Frequency Tracking and Steady State Performance

It is important to evaluate the effect of SFA mechanism on the frequency-tracking as well as the steady state performance of a PLL. It might seem that the SFA will slow down the speed of frequency tracking or it achieves the mitigation of phase lag at the cost of degraded steady state performance. Both these concerns are invalidated as follows.

Fig. 17 compares the response of the standard SOGI-PLL and the proposed SFA-SOGI-PLL during a step change of 5 Hz in the input voltage frequency. Compensator  $H_{PLL}(s)$  for both the PLLs are identical and selected from Table I for 30 Hz bandwidth design. It is evident from Fig. 17 that the proposed SFA-SOGI-PLL significantly improves damping and does not slow down the speed of frequency tracking.

Because in the steady state the frequency input to an OSG for PLL with or without the SFA mechanism are equal, the proposed PLLs with SFA of OSG preserve the steady-state performance of standard PLL structures. For example, Fig. 18 compares the steady state response of a standard SOGI-PLL and the proposed SFA-SOGI PLL in the presence of a 5% third harmonic in the input voltage,  $v_{ac}$ . It is evident that both the PLLs experience the same level of distortion in steady state in the estimated frequency output. This confirms that the SFA of OSG improves transient performance and eliminates the bandwidth limit of single-phase SRF-PLLs without affecting their steady state performance. Obviously, because SFA does not improve or degrade the steady state behavior, increasing the bandwidth of a PLL using SFA will also increase distortions in the PLL output if the input voltage is polluted, same as expected from a standard PLL; however,

mitigating the effects of harmonic pollution as the PLL bandwidth is increased is a separate problem whose severity is unaffected by the proposed SFA mechanism. Many modifications have been proposed recently in the literature for standard PLL structures to improve their performance in the presence of harmonics and dc-offsets [28]; all these methods are equally applicable to PLLs with SFA of OSG.

## V. CONCLUSION

This paper introduced harmonic signal-flow graphs for LTP systems to streamline the modeling of grid-connected converters by visually describing the flow of sinusoidal perturbations through the circuit and control system of a converter. The paper demonstrated modeling using harmonic signal-flow graphs for two commonly used single-phase PLLs based on the SRF architecture: SOGI-PLL and Park-PLL. It is shown using the developed loop gain models of these PLLs that interaction with the orthogonal signal generator (OSG) in these PLLs introduces a significant phase lag in their loop gains, which limits the maximum bandwidth for which either PLL can be designed. The paper proposed slow-frequency adaptation (SFA) of OSG to decouple the frequency and phase-locking dynamics and eliminate the bandwidth limit. This enables PLL designs with higher bandwidths and faster response. Experimental results are presented to verify the stability predictions of the developed loop-gains models and show that the proposed SFA of OSG eliminates the bandwidth limit and significantly improves the transient performance of single-phase SRF-PLLs without degrading their steady-state performance.

## ACKNOWLEDGEMENTS

This work was authored in part by Alliance for Sustainable Energy, LLC, the manager and operator of the National Renewable Energy Laboratory for the U.S. Department of Energy (DOE) under Contract No. DE-AC36-08GO28308. Funding provided by U.S. Department of Energy Office of Energy Efficiency and Renewable Energy Solar Energy Technologies Office. The views expressed in the article do not necessarily represent the views of the DOE or the U.S. Government. The U.S. Government retains and the publisher, by accepting the article for publication, acknowledges that the U.S. Government retains a nonexclusive, paid-up, irrevocable, worldwide license to publish or reproduce the published form of this work, or allow others to do so, for U.S. Government purposes.

## REFERENCES

- [1] S. Shah and L. Parsa, "Impedance modeling of three-phase voltage source converters in dq, sequence, and phasor domains," *IEEE Trans. Energy Conv.*, vol. 32, no. 3, pp. 1139-1150, Sept. 2017.
- [2] L. Harnefors, M. Bongiorno, and S. Lundberg, "Input-admittance calculation and shaping for controlled voltage-source converter," *IEEE Trans. Ind. Electron.*, vol. 54, no. 6, pp. 3323-3334, Dec. 2007.
- [3] S. Shah and L. Parsa, "On impedance modeling of single-phase voltage source converters" in *Proc. 2016 IEEE Energy Conv. Cong & Expo.*, Milwaukee, WI.
- [4] L. Harnefors, X. Wang, A. G. Yepes, and F. Blaabjerg, "Passivity-based stability assessment of grid-connected VSCs – an overview," *IEEE J. Emerg. Sel. Topics Power Electron.*, vol. 4, no. 1, pp. 116-125, Mar. 2016.
- [5] E. Mollerstedt, "Dynamic analysis of harmonics in electrical systems," Ph.D. dissertation, Lund Inst. Technology, Sweden, 2000.
- [6] S. R. Hall and N. M. Wereley, "Generalized nyquist stability criterion for linear time periodic systems," in *Proc. 1990 Amer. Control Conf.*, pp. 1518-1525, San Diego, CA.
- [7] R. D. Middlebrook, "Describing function properties of a magnetic pulsewidth modulator," *IEEE Trans. Aerosp. Electron. Syst.*, vol. AES-9, no. 3, pp. 386-398, May 1973.

- [8] J. Sun and K. J. Karimi, "Small-signal input impedance modeling of line-frequency rectifiers," *IEEE Trans. Aerosp. Electron. Syst.*, vol. 44, no. 4, pp. 1489-1497, Oct. 2008.
- [9] Z. Bing, K. J. Karimi, and J. Sun, "Input impedance modeling and analysis of line-commutated rectifiers," *IEEE Trans. Power Electron.*, vol. 24, no. 10, pp. 2338-2346, Oct. 2009.
- [10] J. Sun, Z. Bing, and K. J. Karimi, "Input impedance modeling of multipulse rectifiers by harmonic linearization," *IEEE Trans. Power Electron.*, vol. 24, no. 12, pp. 2812-2820, Dec. 2009.
- [11] V. Salis, A. Costabeber, S. M. Cox, and P. Zanchetta, "Stability assessment of power-converter-based ac systems by LTP theory: eigenvalue analysis and harmonic impedance estimation," *IEEE J. Emerg. Sel. Topics Power Electron.*, vol. 5, no. 4, pp. 1513-1525, Dec. 2017.
- [12] V. Salis, A. Costabeber, S. M. Cox, P. Zanchetta, and A. Formentini, "Stability boundary analysis in single-phase grid-connected inverters with PLL by LTP theory," *IEEE Trans. Power Electron.*, vol. 33, no. 5, pp. 4023-4036, June 2017.
- [13] J. Kwon, X. Wang, F. Blaabjerg, C. L. Bak, A. R. Wood, and N. R. Watson, "Harmonic instability analysis of single-phase grid-connected converter using harmonic state-space (HSS) modeling method," *IEEE Trans. Ind. Appln.*, vol. 52, no. 5, pp. 4188-4200, Sep./Oct. 2016.
- [14] J. Lyu, X. Zhang, X. Cai, and M. Molinas, "Harmonic state-space based small-signal impedance modeling of modular multilevel converter with consideration of internal harmonic dynamics," *IEEE Trans. Power Electron.*, vol. 34, no. 3, pp. 2134-2148, May 2018.
- [15] Middlebrook, "Topics in multiple-loop regulators and current-mode programming," *IEEE Trans. Power Electron.*, vo. PE-2, no. 2, pp. 109-124, April 1987.
- [16] S. Shah and L. Parsa, "Large-signal impedance for the analysis of sustained resonance in grid-connected converters," in *Proc. of 2017 IEEE COMPEL Workshop*, July 2017.
- [17] S. Shah and L. Parsa, "Impedance-based prediction of distortions generated by resonance in grid-connected converters," *IEEE Trans. Energy Conv.*, vol. 34, no. 3, pp. 1264-1275, Sep. 2019.
- [18] S. Shah, P. Koralewicz, V. Gevorgian, R. Wallen, K. Jha, D. Mashtare, R. Burra, and L. Parsa, "Large-signal impedance-based modeling and mitigation of resonance of converter-grid systems," *IEEE Trans. Sustain. Energy*, vol. 10, no. 3, pp. 1439-1449, July 2019.
- [19] R. Teodorescu, M. Liserre, and P. Rodriguez, *Grid Converters for Photovoltaic and Wind Power Systems*. Chichester, UK: Wiley, 2011.
- [20] Y. Han, M. Luo, X. Zhao, J. M. Guerrero, and L. Xu, "Comparative performance evaluation of orthogonal-signal-generators based single-phase PLL algorithms - a survey," *IEEE Trans. Power Electron.*, vol. 31, no. 5, pp. 3932-3944, May 2016.
- [21] S. Golestan, J. M. Guerrero, A. Vidal, A. G. Yepes, J. Doval-Gandoy, and F. D. Freijedo, "Small-signal modeling, stability analysis and design optimization of single-phase delay-based PLLs," *IEEE Trans. Power Electron.*, vol. 31, no. 5, pp. 3517-3527, May 2016.
- [22] S. Golestan, M. Monfared, F. D. Freijedo, and J. M. Guerrero, "Dynamics assessment of advanced single-phase PLL structures," *IEEE Trans. Ind. Electron.*, vol. 60, no. 6, pp. 2167-2177, June 2013.
- [23] P. Rodriguez, A. Luna, I. Candela, R. Muijal, R. Teodorescu, and F. Blaabjerg, "Multiresonant frequency-locked loop for grid synchronization of power converters under distorted grid conditions," *IEEE Trans. Ind. Electron.*, vol. 58, no. 1, pp. 127-138, Jan. 2011.
- [24] P. Rodriguez, A. Luna, R. S. Munoz-Aguilar, I. Etxeberria-Otadui, R. Reodorescu, and F. Blaabjerg, "A stationary reference frame grid synchronization system for three-phase grid-connected power converters under adverse grid conditions," *IEEE Trans. Power Electron.*, vol. 27, no. 1, pp. 99-112, Jan. 2012.
- [25] S. Golestan, J. M. Guerrero, and J. C. Vasquez, "Higher-order frequency-locked loops: a critical analysis," *IEEE Trans. Power Electron.*, vol. 32, no. 5, pp. 3285-3291, May 2017.
- [26] F. Xiao, L. Dong, L. Li, and X. Liao, "A frequency-fixed SOGI-based PLL for single-phase grid-connected converters," *IEEE Trans. Power Electron.*, vol. 32, no. 3, pp. 1713-1719, Mar. 2017.
- [27] R. Walton. *Mason.m* (2000) [Online]. Available: <http://www.mathworks.com/matlabcentral/fileexchange/22-mason-m>
- [28] S. Golestan, J. M. Guerrero, and J. C. Vasquez, "Single-phase PLLs: a

review of recent advances,” *IEEE Trans. Power Electron.*, vol. 32, no. 12, pp. 9013-9030, Dec. 2017.



**Shahil Shah** (S’13–M’18) received the B.E. degree from Government Engineering College, Gandhinagar, India, in 2006, the M.Tech. degree from the Indian Institute of Technology (IIT) Kanpur, Kanpur, India, in 2008, and the Ph.D. degree from Rensselaer Polytechnic Institute (RPI), Troy, NY, in 2018, all in Electrical Engineering.

Before joining the Ph.D. program at RPI in 2012, he worked in India at Bhabha Atomic Research Center, Siemens Corporate Technology, and GE Global Research Center. Currently he is a Research Engineer in the Power Systems Engineering Center of the National Renewable Energy Laboratory (NREL), Golden, CO. His research interests include applications of modeling and control for dynamic and transient stability of power systems with high penetration of renewable generation.

Dr. Shah was the recipient of the 2018 RPI Allen B. Dumont prize, given to a doctoral candidate “who demonstrates high scholastic ability and makes substantial contribution to his/her field.”



**Przemyslaw Koralewicz** (M’17) received his MSEE from Silesian Technical University in Gliwice, Poland in 2010. He specializes in modeling, detailed analysis and testing of smart inverters and complex power systems including microgrids. He is utilizing the NREL Controllable Grid Interface (CGI), a new, groundbreaking testing apparatus and methodology to test and demonstrate many existing and future advanced controls for various renewable generation technologies on the multimewatt scale and medium-voltage levels.



**Vahan Gevorgian** (M’97–SM’17) received the Ph.D. degree in electrical engineering from the State Engineering University of Armenia, Yerevan, Armenia, in 1993. He joined NREL in October 1994 and has served many roles over the years. He is currently working with the Power Systems Engineering Center focused on renewable energy impacts on transmission and interconnection issues and dynamic modeling of variable generation systems. He is involved in many different areas

including dynamometer and field testing of large and small wind turbines, dynamometer testing of wind turbine drivetrain components, development of advanced data acquisition systems, and wind turbine power quality. Vahan provides technical support to NREL industry partners and major U.S. wind turbine manufacturers. He is member of the IEC team for wind turbine power quality standards. His contributions to NREL research have been recognized through multiple Outstanding Individual and Team Staff Awards.



**Leila Parsa** (S’00–M’05–SM’10) received the Ph.D. degree in Electrical Engineering from Texas A&M University, College Station, TX in 2005. She is currently a professor in the department of electrical and computer engineering at University of California, Santa Cruz. From 2005 to 2016 she was a faculty member in the department of Electrical, Computer, and Systems Engineering at Rensselaer Polytechnic Institute, Troy, NY. Her research interests are in design, analysis and control of electromechanical

energy converters and power electronics converters for various applications.

Dr. Parsa was the recipient of several awards including the 2009 Office of Naval Research Young Investigator Award, the 2007 IEEE Industry Applications Society Outstanding Young Member Award, and 2006 IEEE Industry Applications Society Transactions Paper Award. Dr. Parsa has authored or co-authored over 100 journal and conference publications. She has served in technical program committee of several IEEE conferences and acted as a technical program co-chair of IEEE International Electric Machines and Drives Conference in 2015. Currently She is an associate editor of IEEE Transactions on Industry Applications and an editor of IEEE Transactions on Energy Conversion.